Effect of periodicity on the magnetic anisotropy in spinel oxide superlattices

Federico Motti,[1,2,*] Lauren J. Riddiford,[1,2] Diana Vaclavkova,[2] Sourav Sahoo,[1,2] Arnold Milenko Müller,[3] Christof Vockenhuber,[3] Ali Baghi Zadeh,[4] Cinthia Piamonteze,[2] Christof W. Schneider,[2] Valerio Scagnoli,[1,2] and Laura J. Heyderman[1,2]

[1]*Laboratory for Mesoscopic Systems, Department of Materials, ETH Zurich, 8093 Zurich, Switzerland*
[2]*Paul Scherrer Institute, 5232 Villigen PSI, Switzerland*
[3]*Laboratory of Ion Beam Physics, Department of Physics, ETH Zurich, 8093 Zurich, Switzerland*
[4]*Scientific Center for Optical and Electron Microscopy, ETH Zurich, 8093 Zurich, Switzerland*

(Received 31 March 2023; accepted 14 August 2023; published 28 September 2023)

Metamaterials, fabricated by assembling different compounds at the nanoscale, can have properties not found in naturally occurring materials, and therefore offer new avenues to develop novel devices. In the realm of spintronics, where the spin of the electrons is used to extend the capabilities of electronic devices, the quest for such new functional materials has expanded towards magnetic oxides. Here, finding methods to control their magnetic anisotropy is crucial to achieve higher memory density and longer stability. In order to address this challenge, we combined two oxides with a spinel crystal structure, synthesizing $CoCr_2O_4/CoFe_2O_4$ superlattices with layers only few unit cells thick. We show that the superlattices present a reorientation of the magnetic easy axis from in plane to out of plane when warmed up, at a temperature determined by the periodicity. We can describe this with a model that includes the strain-induced anisotropy of the two materials and their different temperature dependence. This approach to create artificial materials, involving engineering superlattices to tailor the magnetic anisotropy, can be generalized to a wide range of compounds that can be grown strained on suitable substrates.

DOI: 10.1103/PhysRevB.108.104426

I. INTRODUCTION

The advent and rise of spintronics, i.e., technologies that utilize the spins in a magnetic material to store, manipulate, and carry information [1,2], has fueled the study of magnetic materials and phenomena in the last 30 years. A constant challenge associated with meeting the increasing demand for larger data-storage capacity and more efficient energy consumption is to improve the properties of constituent materials towards better functionality [3,4]. Amongst possible magnetic materials, oxides have gained significant attention, as they can host exotic quantum phases [5], give improvements in the performance of magnetic tunnel junctions [6], enable efficient electric-field switching [4,7–10], and act as the functional element in magnon-based devices [11,12].

Oxides are usually characterized by several interactions competing at a relatively small energy scale, with people often referring to the "interplay of charge, spin, and orbital degrees of freedom" [13]. Therefore, their properties can be very sensitive to external stimuli and preparation conditions, which is appealing not only for the discovery of new phenomena, but also for the optimization of their properties for applications [14]. For this, a flexible and powerful approach is to interface different oxides at the nanoscale, resulting in metamaterials with unique properties that are different from their building blocks [15,16]. With current thin-film deposition techniques, an exquisite control of the growth processes can be achieved, allowing the realization of crystalline oxide superlattices with an atomic control of the thickness [17–19]. Indeed, many impressive results have been achieved in perovskite superlattices systems, such as near room-temperature multiferroicity [20], the formation of ferroelectric vortices [21], the tuning of metal-insulator transitions [22], induced ferromagnetism [23], phases resembling quantum-spin liquids [24], and reversible structural transformations [25].

Following this approach, we have realized superlattices of oxides with a spinel structure [26–29]. The general chemical formula is AB_2O_4. In normal spinels, A ions sit on tetrahedral sites and B ions sit on octahedral sites. There are also inverse spinels, where A ions occupy half of the octahedral sites, while B ions occupy the other half of the octahedral sites, as well as all the tetrahedral sites. We have coupled two different magnetic materials: the normal spinel cobalt chromite ($CoCr_2O_4$, or CCO), a ferrimagnet with a multiferroic phase at low temperature, and the inverse spinel cobalt ferrite ($CoFe_2O_4$, or CFO), a collinear ferrimagnet with high Curie temperature and high magnetostriction. We have monitored the magnetic anisotropy in the CCO/CFO superlattices on changing the periodicity with magnetometry. Using x-ray magnetic circular dichroism (XMCD), we have resolved the magnetization of the two layers as a function of temperature and applied magnetic field. We find that the magnetic easy axis is in the film plane at low temperature and rotates out of plane in an intermediate temperature range, which can be controlled by tuning the thickness of the layers. This temperature evolution is absent in single layers and doped

*Now at: Istituto Officina dei Materiali CNR-IOM, Area Science Park, Strada Statale 14 km 163.5, 34149 Basovizza, Trieste, Italy; motti@iom.cnr.it

 ©2023 American Physical Society

TABLE I. Deposition conditions of the superlattices.

Deposition temperature	550 °C
Deposition O_2 pressure	2×10^{-3} mbar
Cooldown O_2 pressure after deposition	100 mbar
Cooling rate after deposition	30 °C/min
Laser spot size	2.25 mm^2
Energy density	1.5 J/cm^2
Repetition rate	8 Hz
Substrate-target distance	4.5 cm

thin films, and hence is unique to the superlattice structure. To explain this behavior one has to consider: (i) the magnetostriction of CCO and CFO, which would result in perpendicular easy axes for the two materials, (ii) the temperature dependence of the strain-induced magnetic anisotropy, and (iii) the strong exchange coupling at the CCO/CFO interface, which favors the antiparallel alignment of the magnetizations of the two materials.

II. SYNTHESIS AND STRUCTURAL CHARACTERIZATION

CCO/CFO superlattices were synthesized on MgO(001) substrates by pulsed laser deposition. We used a KrF excimer laser (Coherent 201 Pro), providing 20-ns laser pulses with 248-nm wavelength, to ablate $CoCr_2O_4$ and $CoFe_2O_4$ commercial targets (SurfaceNet and K.J. Lesker, respectively). The deposition conditions are summarized in Table I.

We have grown single layers of CCO and CFO on MgO(001) in identical conditions, and determined their thickness by fitting x-ray reflectometry data. In this way we obtain the deposition rate of the two materials. We then deposited CFO/CCO superlattices by ablating alternatively the two targets with a number of laser pulses that would result in the desired thickness and periodicity. Superlattices of the form [CFO(N unit cells, u.c.)/CCO (Mu.c.)]$_n$/MgO(001) are referred to as SL *N/M*. The number of repetitions n was adjusted in order to have a total thickness around 80 nm. For the spinel crystal structure, a unit cell is composed of four different atomic layers. Therefore, it is possible to deposit films with a thickness that is a fraction of a unit cell. Here, we focus on a series of samples with varying N, and with the constraint $M = 4N$. In particular, we will discuss superlattices SL 0.5/2, SL 0.75/3, SL 1/4, SL 2/8, and SL 4/16. We also synthesized solid solutions of $Co(Cr_{1-x}Fe_x)_2O_4$, by alternating the ablation of CCO and CFO targets, with the number of pulses giving a submonolayer thickness (i.e., less than 0.25 u.c.).

We determined the structural quality of the samples with x-ray diffraction. The diffraction data were acquired with a Bruker D8 diffractometer, equipped with a microfocused and monochromatic Cu $K_{\alpha 1}$ source ($\lambda = 1.54$ Å), and the results are summarized in Fig. 1. First, we verified the quality of the superlattices with coupled 2θ–ω scans around the MgO(002) Bragg peak. In Fig. 1(a), one can see the superlattice (004) peak surrounded by satellite peaks. The satellite peaks are the result of the constructive interference from the periodic modulation of the out-of-plane lattice constant of the superlattice, and their presence testifies that the interfaces between the different layers are sharp. The Bragg peak to satellite distance in reciprocal space corresponds to $\Delta Q_z = 2\pi/d$, from which the the period of the superlattice, d, can be calculated. Although the value of d obtained may vary up to 10% from the nominal one, the members of the series of samples realized have clearly distinct periodicity.

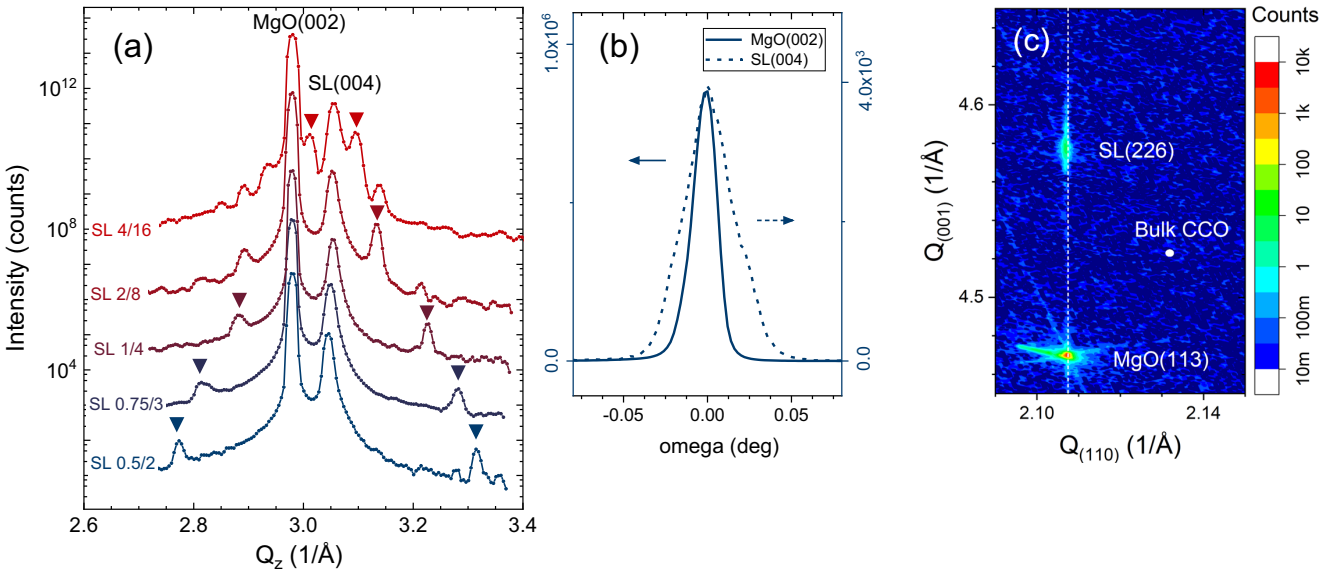

FIG. 1. X-ray diffraction characterization of superlattices grown on MgO(001) substrates. (a) Coupled 2θ–ω scans around the MgO(002) Bragg peak. Arrowheads indicate first-order satellites of the superlattice, from whose position, relative to the main peak, the period was calculated. (b) Omega scans on the MgO(002) and film(004) Bragg peaks of SL 0.5/2. The similar width of the peaks imply that the density of defects in the film is similar to the density of defects in the substrate. (c) Reciprocal space map around the MgO(113) Bragg peak of SL 0.5/2, showing that the in-plane lattice parameter of the film matches the one of the substrate. The white dot indicates the expected position of the (226) reflection for bulk CCO.

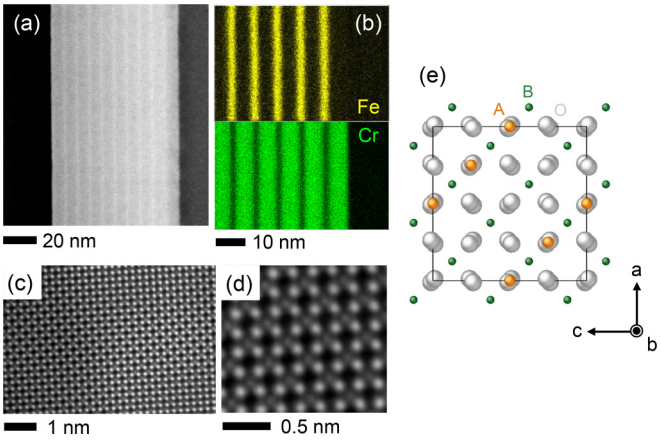

FIG. 2. (a) STEM image of a cross section of the SL 2/8 sample acquired with a HAADF detector, from which we can distinguish the different layers in the superlattice. (b) EDS mapping of the region close to the interface, showing signal at the Fe *K* edge (above) and at the Cr *K* edge (below). The Fe- and Cr-rich layers look well separated, with minimal mixing at the interfaces. (c), (d) Higher-magnification HAADF images, showing the typical spinel crystal structure. (e) Schematic of the spinel unit cell. Atoms labeled A sit on tetrahedral sites (Co in CCO, Fe in CFO) while atoms labeled B sit on octahedral sites (Cr in CCO, Co and Fe in CFO). The orientation of the crystal is the same for all panels in this figure.

The full width at half maximum (FWHM) of a Bragg peak in a rocking scan is a common way to assess the structural quality of crystalline materials, since it is determined by the density of dislocations and by crystallographic planes that are not perfectly oriented. In our superlattice, the rocking scan of the spinel (004) peak has a FWHM of approximately 0.02°, which is the same order of magnitude as the width of substrate MgO(002) peak [see Fig. 1(b)]. This confirms that the films grow with low defect concentration, comparable to that of the substrate.

In order to determine the in-plane lattice parameter of our superlattices, we have acquired reciprocal space maps around the MgO(113) Bragg peak. As shown in Fig. 1(c), the superlattice (226) peak aligns to the substrate peak along the in-plane [110] coordinate. Therefore, the films have an in-plane lattice parameter which matches that of the substrate, and we see no evidence of relaxation towards the bulk lattice parameter.

With scanning transmission electron microscopy (STEM), we confirm the high structural quality of the superlattices. Lamellas were cut out of the samples using a focused ion beam and observed in cross section with a double-corrected JEOL GrandARM microscope, operated at 200 kV. Images for SL 2/8 are shown in Fig. 2 and for SL 1/4 are given in the Supplemental Material [31]. High-angle annular dark-field (HAADF) images display a clear contrast reflecting the different atomic composition of the layers [Fig. 2(a)]. Furthermore, energy-dispersive spectroscopy (EDS) was used for elemental mapping, and a clear separation of the signal originating from Fe and Cr atoms is seen [Fig. 2(b)], confirming the periodic structure of the samples evidenced by x-ray diffraction. With higher-resolution images, it is possible to visualize the individual atoms and to recognize the typical spinel structure [Figs. 2(c) and 2(d)] [30]. However, some defective regions have been observed by STEM, as shown in the Supplemental Material [31] (Figs. S9 and S10).

III. MAGNETIC PROPERTIES

The magnetic properties of the samples were characterized with a Superconductive Quantum Interface Device–Vibrating Sample Magnetometer (SQUID-VSM, model MPMS 3, Quantum Design). To measure the temperature dependence of the magnetization, the samples were first cooled down to a base temperature of 5 K in a magnetic field larger than the saturation field of the sample. Then, the magnetization as a function of temperature $M(T)$ was measured while warming up the sample in a magnetic field of 20 mT. This is equivalent to measuring the magnetization close to remanence at each temperature following saturation. The same procedure was repeated with the magnetic field parallel and perpendicular to the film plane, corresponding to the crystallographic directions [100] and [001], respectively. The component of the magnetization vector measured is always the one parallel to the field.

We begin by summarizing the magnetic properties of thin films of CCO and CFO, as known from the literature. The Curie temperature of bulk CCO is 95 K and its magnetization is reported to be less than 0.2 μ_B per formula unit [32,33]. The spins arrange in a spin cycloid below 27 K, thus breaking space-inversion symmetry and inducing a small electrical polarization coupled to the magnetic order [32,34–37]. This means that CCO is a multiferroic (i.e., a material that is ferroelectric and has a net magnetic moment), which is very rare. In comparison, bulk CFO has a Curie temperature larger than 700 K, a collinear spin structure, and a magnetization that is one order of magnitude larger than CCO [38].

Due to the mismatch of lattice constants, both CCO and CFO films are under tensile strain when grown on MgO substrates. However, the magnetostriction coefficients of the two compounds have opposite signs. Thus, the out-of-plane direction is the magnetic easy axis for CFO thin films, but is the magnetic hard axis for CCO [39,40]. The $M(T)$ data for simple CCO and CFO thin films are presented in Fig. S2(a) in the Supplemental Material [31], and are consistent with the results reported in the literature. However, it is worth mentioning that we could not observe the magnetic Bragg peak corresponding to the spin cycloid in CCO using resonant x-ray scattering at the SIM beamline of the Swiss Light Source, for any of the samples that we grew under different conditions (see Supplemental Material [31], Fig. S3). Rutherford backscattering measurements revealed a deviation from the ideal stoichiometry in the thin films (see Supplemental Material [31], Table S1), which could be responsible for the absence of the low-temperature multiferroic phase.

To compare the magnetic properties of the superlattices, which have a modulated structure, with the uniform compound, we measured the magnetization of doped $Co(Cr_{1-x}Fe_x)_2O_4$ thin films, with the $M(T)$ data reported in the Supplemental Material [31] [Fig. S2(b)]. We observed that the Curie temperature increases with x, as reported for powder samples [41–43]. For $x = 0.2$ (corresponding to the

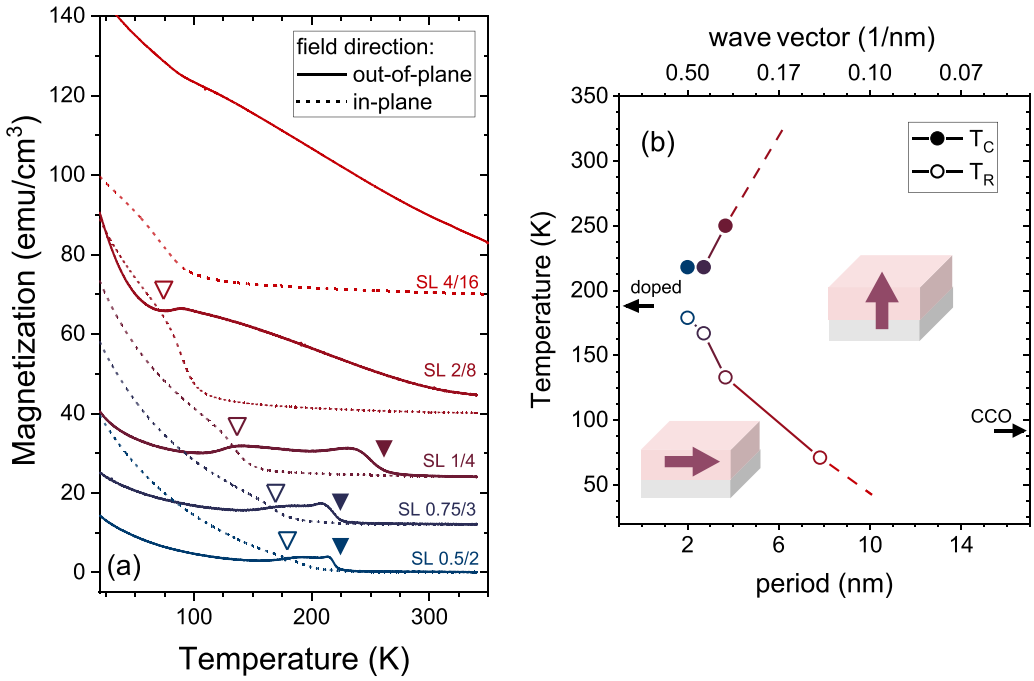

FIG. 3. Magnetic characterization of the superlattices by SQUID-VSM. (a) Magnetization as a function of temperature, measured while heating in an applied magnetic field of 20 mT, after field cooling. Solid lines correspond to measurements carried out along the out-of-plane direction (001), and dashed lines to measurements carried out along the in-plane direction (100). Curves corresponding to different samples are offset for clarity. For each sample, the dashed lines go to zero on the high-temperature side. Filled arrowheads indicate T_C, and unfilled triangles indicate T_R. (b) The detected transition temperatures for superlattices with different periodicity. The measured period for the various SL N/M samples is indicated in nm with 1 u.c. ≈ 0.83 nm. Between T_C and T_R, the magnetization easy axis is out-of-plane, while below T_R it is in-plane. The Curie temperature of bulk CCO and of the doped $Co(Cr_{0.8}Fe_{0.2})_2O_4$ thin films are indicated with black arrows. In panel (b), the lines are a guide to the eye and dashed lines represent a qualitative extrapolation based on the fact that the SL with large periods have $T_C > 350$ K, and $T_R \to 0$ K.

same Cr/Fe ratio of $M/N = 4$ used in the SL samples), the magnetization is higher when measured in plane compared to the magnetization measured out of plane for the whole temperature range below the Curie temperature [Fig. S2(a)]. Therefore, the $x = 0.2$ doped thin film is characterized by an in-plane magnetic anisotropy.

In contrast to the doped samples, the superlattices exhibit a complex temperature dependence of their magnetic anisotropy, which is also distinct from either of the parent materials. The results of the magnetization measurements for the superlattices are summarized in Fig. 3. In Fig. 3(a), we see that at low temperature, the magnetization measured with the magnetic field in plane is on the whole higher than for the out-of-plane case, similar to that observed for pure CCO (Fig. S2). As the temperature increases, the out-of-plane magnetization increases at the expense of the in-plane one, which drops abruptly, and we observe a reorientation of the direction of the magnetization from in plane to out of plane at a temperature T_R (the reorientation temperature is indicated with unfilled arrowheads). T_R was determined as the crossing point between the $M(T)$ curves acquired for magnetic field applied in the two orthogonal directions. Finally, at a temperature T_C (indicated with filled arrowheads) the out-of-plane magnetization also goes to zero. T_C corresponds to the minimum of the first derivative dM/dT for magnetic field applied out of plane, and can be interpreted as the Curie temperature of the sample. Sample SL 4/16 is an exception, since the out-of-plane magnetization is always higher than the in-plane magnetization. Nevertheless, we observe a sharp decrease of the in-plane magnetization with a corresponding change in slope in the out-of-plane magnetization, similar to that observed in the other samples in the proximity of T_R.

In summary, with this magnetic characterization, we show that the superlattices display a change in magnetic anisotropy as a function of temperature, which is not observed in doped samples, and does not emerge trivially from the individual properties of the single layers. The temperature range corresponding to an out-of-plane easy axis depends on the thickness of the layers, and hence can be tailored by modifying the design of the superlattice.

IV. SPECTROSCOPIC MEASUREMENTS WITH SYNCHROTRON X-RAYS

In order to disentangle the contribution of the different layers to the overall magnetic properties measured by SQUID-VSM, we have collected XMCD spectra at the $L_{2,3}$ edges of Cr, Fe, and Co. These measurements were performed at the Xtreme endstation of the X07MA beamline at the Swiss Light Source [44]. Here, absorption spectra were collected via x-ray excited optical luminescence of the MgO substrate, which gives a bulk-sensitive measurement equivalent to transmission detection [45,46]. XMCD spectra are calculated as the difference between absorption spectra collected with left and right

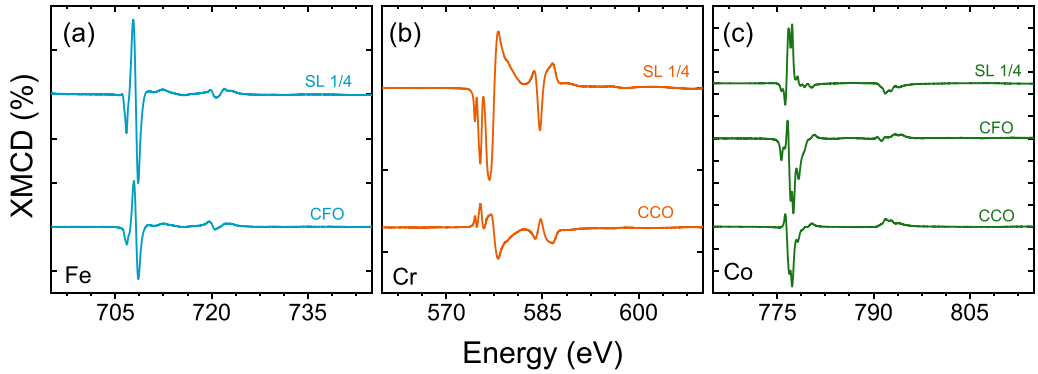

FIG. 4. XMCD spectra acquired for pure CCO and CFO thin films, and the SL 1/4 superlattice. All spectra were collected in a 6.8-T magnetic field applied parallel to the x-ray beam at 20 K. The angle of incidence of x-rays was 90° for CFO, and 30° for both CCO and SL 1/4, so that the magnetic field, which is fixed along the x-ray beam direction, is parallel to the easy axis for each sample. Data corresponding to different samples are offset for clarity. All spectra start on the left at 0, and the ticks in the vertical axes of all panels are separated by 10%. The XMCD spectra are recorded at the (a) Fe $L_{2,3}$ edges, (b) Cr $L_{2,3}$ edges, and (c) Co $L_{2,3}$ edges.

circularly polarized x rays. The intensity of the signal obtained is a measure of the (element-resolved) magnetic moment projected on the direction of the propagating x rays.

In a first step, we determine the orientation of the magnetic moment of the various ions in the superlattice. Typical spectra are shown in Fig. 4 for the single layers and the SL 1/4, all taken at 20 K. The meaning of the % scale for the XMCD intensity is explained in the Supplementary Material, Sec. 5 [31]. A magnetic field of 6.8 T was applied along the x-ray direction in order to measure the saturation magnetic moment of the samples. Since we have applied a strong magnetic field, the magnetization will be parallel to it in each case. The sign of the XMCD spectra of a particular element then tells us the direction of the magnetic moment with respect to the external field. In both CCO and CFO, the Co spins orient parallel to the applied magnetic field. This gives a negative XMCD at the Co L_3 edge as observed for the two isolated thin films [Fig. 4(c)]. In CFO, Fe ions sit on both octahedral and tetrahedral sites. Those on the octahedral sites have a spin parallel to the magnetic field, while for those on the tetrahedral sites the spin is antiparallel to the magnetic field. Since the x-ray absorption spectra for Fe on the two sites are not identical, a nonzero XMCD is observed. This gives a typical spectrum for CFO with three peaks of alternating XMCD sign at the Fe L_3 edge [Fig. 4(a)]. In CCO thin films, Cr spins sitting on the octahedral sites are antiparallel to the Co spins and to the magnetic field. This results in an XMCD at the Cr L_3 edge with three positive peaks followed by a negative one [Fig. 4(b)]. Our XMCD data for the SL samples show that the magnetization of the CCO and CFO layers are antiparallel to each other. Indeed, we find that the Fe XMCD spectra for SL 1/4 and the pure CFO have the same shape [Fig. 4(a)], while the sign of the Cr XMCD for the superlattice is reversed compared to that of the pure CCO [Fig. 4(b)]. This means that the Fe magnetic moments in the superlattice are oriented as in the simple CFO thin film, and therefore the CFO layers in SL have a magnetization parallel to the external field. In contrast, the Cr magnetic moments in SL 1/4 are antiparallel to those in the simple CCO thin film, when subject to the same saturating magnetic field. We can therefore conclude that the magnetization in the CCO layers in the superlattice is antiparallel to the magnetic field. The signal at the Co $L_{2,3}$ edges in SL 1/4 [Fig. 4(c)] emerges from the Co ions present in both the CCO and CFO layers, since our measurements are bulk sensitive. Based on this discussion, we expect the Co spins in CFO layers to be parallel to the magnetic field (giving a negative XMCD at the L_3 edge) and the Co spins in the CCO layers to be antiparallel to it (giving a positive XMCD at the L_3 edge). Since CCO constitutes 3/4 of the total volume of the superlattice, the signal observed originates mainly from the CCO layers. As a confirmation, we see that the sign of the Co XMCD spectra for SL 1/4 is reversed compared to that of the pure CCO thin film, as for the Cr case. To summarize, the CFO and CCO layers in the superlattice are antiferromagnetically coupled, and the magnetization of CFO is aligned with the external magnetic field. The arrangement of the magnetic moments of the various ions for the different samples is summarized in Table S2 in the Supplemental Material [31].

In a second step, we determine how the magnetic anisotropy of the individual layers in the superlattice contribute to the overall magnetic anisotropy of the sample. The magnetic anisotropy is manifested in the shape of a magnetic hysteresis loop $M(H)$, since the remanence and the coercive field are strongly influenced by the direction of the magnetic field with respect to the easy axis. Therefore, it is possible to qualitatively assess the magnetic anisotropy by measuring $M(H)$ loops for different directions of the magnetic field. One can obtain element-specific hysteresis loops by measuring the XMCD signal at an absorption edge of a particular element while sweeping the magnetic field (experimental details are given in the Supplemental Material [31]). We measured the hysteresis loops at the Fe and Cr L_3 edges for the SL 1/4 superlattice at different temperatures, and for two geometries: normal incidence of the x rays, which is sensitive to the out-of-plane magnetic moment, and 30° angle of incidence of the x rays, which is mostly sensitive to the in-plane magnetic moment. In Figs. 5(a) and 5(b) we compare Fe- and Cr-specific hysteresis loops above and below T_R, at 150 and 20 K, respectively. The loops obtained at the two absorption edges have opposite sign, as expected due to the antiparallel alignment of Cr and Fe moments. Apart from this, their shapes

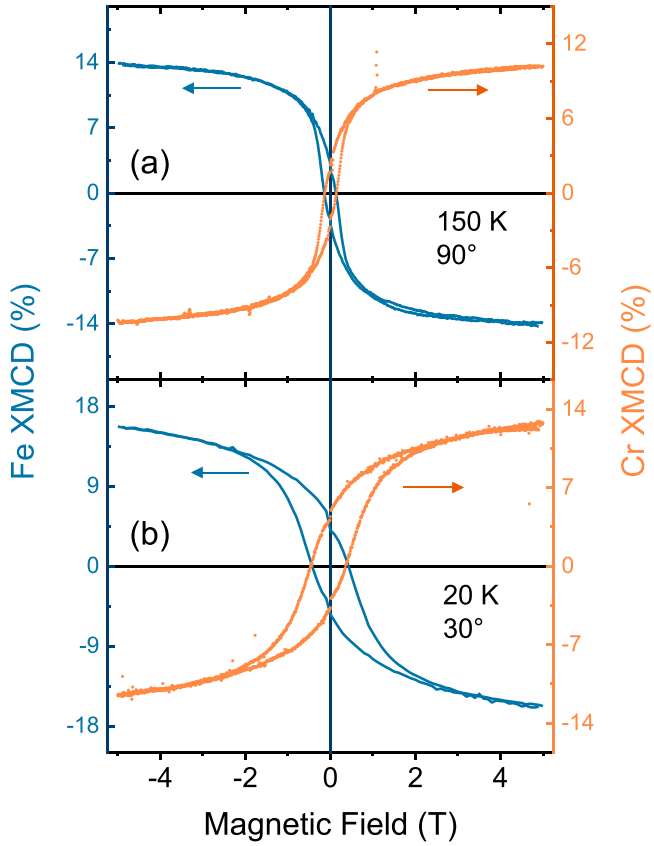

FIG. 5. Element-sensitive magnetic hysteresis loops of SL 1/4 for different temperatures and geometries. (a) Comparison between Fe- and Cr-specific hysteresis loops at 150 K with 90° x-ray angle of incidence. (b) Comparison between Fe- and Cr-specific hysteresis loops at 20 K, with 30° x-ray angle of incidence. For both temperatures the Fe and Cr loops show the same remanence and coercive field.

are the same, which means that the CFO and CCO layers have the same magnetic anisotropy. Otherwise, a difference in remanence or coercive field would be evident. The shape of the hysteresis is different for temperatures above and below T_R [compare Figs. 5(a) and 5(b)], but in both cases the Fe and Cr signals are equal apart from the sign (compare the two curves within each panel). A more detailed comparison for the two temperatures and two geometries is presented in the Supplemental Material [31] (Fig. S5). There, we also show similar data collected for SL 2/8 (Figs. S6 and S7). Overall, we can conclude that the reorientation of the easy axis from in plane to out of plane observed by SQUID-VSM is common to both the CCO and CFO layers in the superlattices.

Finally, after showing the similarities in the magnetic properties of the CFO and CCO layers, we now discuss their differences, which are evident from the temperature dependence of their saturated magnetization. To evaluate this, we measured the Cr and Fe XMCD signals as a function of temperature in a saturating field of 6.8 T, applied at an angle of 30° to the film surface. Four different superlattices were compared: SL 0.5/2, SL 1/4, SL 2/8, and SL 4/16, with all of the results presented in Figs. S8(a) and S8(b) of the Supplemental Material [31]. Both the Cr and Fe XMCD L_3 peak signals decrease smoothly with increasing temperature. However, their relative change is not constant, as evidenced by their ratio [Fig. 6(a)]. In particular, the Cr/Fe XMCD ratio decreases when warming up. Therefore, despite the fact that the preferential direction of the magnetization of the CCO and CFO layers in the superlattice is the same, the magnetization in the CCO layers decrease faster than the magnetization in the CFO layers on increasing the temperature. SL 4/16 shows a unique behavior, since its Cr/Fe XMCD ratio seems to be nonmonotonic, with a local minima around 80 K [Fig. 6(a)], close to the temperature at which the in-plane magnetization goes to zero [Fig. 3(a)]. In general, the decay of the Cr/Fe XMCD ratio on increasing temperature is faster for samples with higher period, and we see that the Fe XMCD is smaller in superlattices with smaller period (thinner layers), while the Cr XMCD is larger. This is shown for $T = 140$ K in Fig. 6(b). A last observation is that, in all superlattices, a Cr XMCD signal is visible above the bulk Curie temperature of 90 K [Fig. S8(b)]. This means that the ordering temperature of the CCO layers in the superlattices is higher than in the bulk. This increased Curie temperature is also higher than T_R, since Cr-sensitive hysteresis loops are detected above T_R (see hysteresis loops taken at 150 K in Figs. 5, S5–S7). Therefore, neither T_C nor T_R as labeled in Fig. 3 corresponds to the Curie temperature of the single CCO and CFO layers. From this, we can infer that our samples display magnetic properties that are unique to the superlattice structure, and emerge from the interaction between the constituents.

V. DISCUSSION

We will first discuss the origin of the observed antiferromagnetic coupling of the CCO and CFO layers, and the temperature dependence of the magnetic properties of the CCO layers. We then formulate a model that describes the observed trends in the magnetic anisotropy of the superlattices.

A. Origin of the antiferromagnetic coupling

The observed antiferromagnetic coupling between the CCO and CFO layers is similar to that between magnetite and chromite in bilayers [47]. This can be explained by considering the microscopic magnetic interactions in spinels. CCO and CFO have magnetic ions both in tetrahedral sites (Co for CCO; Fe for CFO) and octahedral sites (Cr for CCO; both Co and Fe for CFO). According to the current understanding of exchange interactions in spinels [48–50], the magnetic coupling between cations in tetrahedral sites is negligible, because these cations are far away from each other. In addition, the exchange interactions between ions in octahedral sites is antiferromagnetic and also generally quite weak as a result of the almost 90° bond angle. The strongest interaction is the antiferromagnetic exchange coupling between the cations in octahedral and tetrahedral sites, which is responsible for the ferrimagnetic order in bulk CCO and CFO. Indeed, the observed antiparallel alignment of the two layers satisfies this exchange interaction across the CCO/CFO interface, resulting in all the magnetic moments in octahedral sites being antiparallel to all those in tetrahedral sites, throughout the whole thickness of the superlattice.

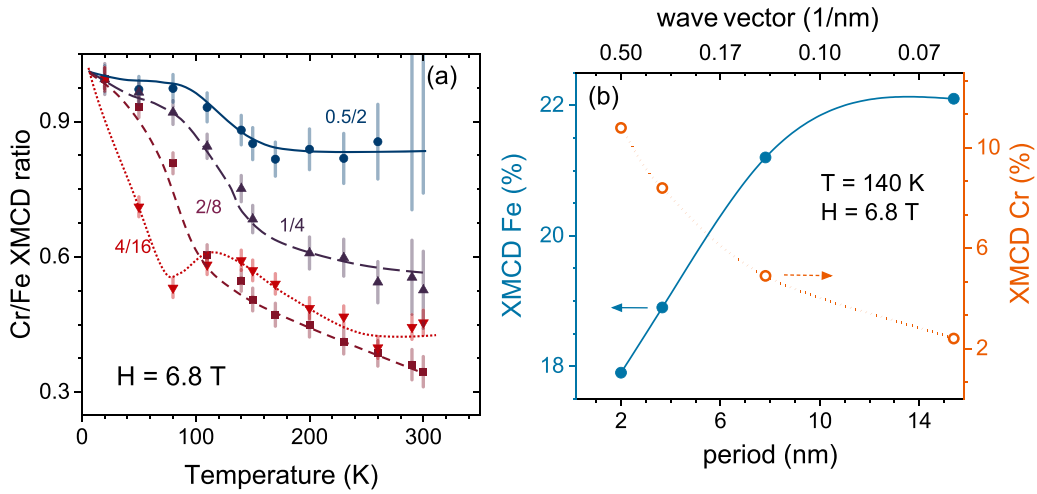

FIG. 6. Trends of the Cr and Fe XMCD L_3-peak signals with temperature for different samples. All data were acquired at a 30° angle of incidence of the x-rays. (a) Cr/Fe XMCD L_3 ratio as a function of temperature, normalized to their value at 20 K. On increasing the temperature, the decrease of the ratio is steeper for samples with higher period. Lines are a guide to the eye. The data without normalization are shown in Fig. S8(c). (b) Fe- and Cr-peak XMCD values at 140 K, for superlattices with different periods. The XMCD increases with period for Fe, but decreases for Cr.

Magnetic films that are very thin often have degraded magnetic properties [51–54]. However, considering the CCO layers in our superlattices, we find that the low-temperature XMCD of Cr is significantly larger than that of the simple thin film [Fig. 4(b)], and it persists above the bulk Curie temperature [Fig. S8(b)]. Indeed, the Cr moment is larger in superlattices with small periods [Fig. 6(b)], characterized by a higher interface/volume ratio. This suggests that the origin of this phenomenon is an interfacial effect. CFO has a higher Curie temperature and larger magnetization than CCO; therefore, the exchange interaction at the CCO/CFO interface can enhance the magnetization of the CCO layers, and induce a magnetic order at temperature higher than in bulk. Because of the interfacial origin of the effect, it makes sense that the detailed temperature dependence of the magnetization of the CCO layers (measured as the Cr XMCD) depends on the periodicity [Fig. 6(a) and Fig. S8].

B. Evolution of magnetic anisotropy

We now turn to the explanation of the reorientation of the easy axis in CCO/CFO superlattices. We have seen that these samples have a magnetic anisotropy that changes with temperature, and that the temperature range where the easy axis is out of plane can be controlled by the periodicity of the superlattice. Hence, their magnetic anisotropy is clearly different from the uniformly doped thin films, as well as the simple thin films of CCO or CFO. Here, we present a simple analytical model that reproduces this behavior, describing the total energy of the system with the following equation:

$$E(\vartheta_A, \vartheta_B) = -K_A t_A \cos^2\vartheta_A + K_B t_B \cos^2\vartheta_B + J_{AB}\, m_A m_B \cos(\vartheta_A - \vartheta_B), \quad (1)$$

where the subscripts A and B refer to CCO and CFO, respectively. $t_{A,B}$ are the thicknesses of the two layers, and $m_{A,B}$ their magnetization. $\vartheta_{A,B}$ are the angles between the magnetization of the layers and the sample plane. The first two terms in the equation represent the strain-induced anisotropy of the two layers [30,55,56] where $K_{A,B}$ are the anisotropy constants, and the opposite signs account for the different magnetostriction in the two layers. A derivation of this expression can be found in Ref. [57]. In writing this equation, we assume that the signs of the anisotropy constants for the CCO and CFO are the same as those of the isolated thin films. This is a reasonable assumption since the origin of this anisotropy is strain. Nevertheless, we make no further assumption about their magnitude. The third term represents the antiferromagnetic coupling between the layers. We can express the microscopic exchange interactions with a Heisenberg Hamiltonian [54], and sum all the interactions across the interface. Assuming that the spins within a material are collinear, the sum gives the third term in Eq. (1), where J_{AB} is an effective average of the microscopic exchange interactions across the interface. The most favorable magnetic configuration is described by the angles $(\vartheta_A, \vartheta_B)$ that give a minimum in the energy $E(\vartheta_A, \vartheta_B)$. If we assume that $J_{AB} \gg K_{A,B}$, which is a reasonable assumption as discussed in the first section of the Supplemental Material [31], the last term is the most important, so we minimize it first. The last term is a minimum when $\cos(\vartheta_A - \vartheta_B) = -1$, i.e., $\vartheta_B = \vartheta_A - \pi$. This means that the magnetizations of the two layers are perfectly antiparallel, which is compatible with the mirrored Cr and Fe hysteresis loops that we observed for the samples SL 1/4 (Fig. 5) and SL 2/8 (Fig. S6). With this constraint, the expression for the energy given by Eq. (1) is reduced to a function with a single angular variable $\vartheta = \vartheta_A$ as follows:

$$E(\vartheta) = -K_A t_A \cos^2\vartheta + K_B t_B \cos^2\vartheta - J_{AB}\, m_A m_B. \quad (2)$$

Equation (2) is an expression for the energy of the whole superlattice as a function of the direction of magnetization in all of the layers. In order to find the stationary points of $E(\vartheta)$, we set the first derivative to be zero:

$$\frac{dE}{d\vartheta} = 2(t_A K_A - t_B K_B)\cos\vartheta \sin\vartheta = 0, \quad (3)$$

which has two solutions, $\vartheta = 0$ and $\vartheta = \pi/2$. To determine whether a stationary point is a maximum or a minimum, we then evaluate the second derivative at that point. If the second derivative is positive, the stationary point is a minimum and, if it is negative, the stationary point is a maximum. We find that $E(0)$ is a minimum and $E(\pi/2)$ is a maximum when $(t_A K_A - t_B K_B) > 0$, which means that the magnetization lies in the plane. In contrast, $E(0)$ is a maximum and $E(\pi/2)$ is a minimum if $(t_A K_A - t_B \mathrm{K}_B) < 0$, which means that the magnetization is out of plane. Therefore, the easy axis for our superlattice can be either in plane or out of plane. Whether either of these two cases is realized depends on the thickness t and the anisotropy constant K of the two materials. However, we observe something in addition: a reorientation of the easy axis as a function of temperature. We now discuss why this occurs.

Our XMCD data have shown that the Cr/Fe XMCD ratio is not constant [Fig. 6(a)], and that the Cr magnetic moment (m_A) has a stronger temperature dependence than the Fe moment (m_B). A decreasing magnetization with temperature is also associated with a decreasing K [55,58]. Therefore, we can imagine that the term $(t_A K_A - t_B K_B)$ is not constant, but will change sign at a certain temperature T_R, which means that the magnetization direction that minimizes the energy can change from in plane to out of plane. Therefore, this model explains the reorientation of the easy axis observed. The specific value of T_R will depend on the thicknesses, and the details of the $K(T)$ dependence. Magnetic interactions across the CCO/CFO interface result in an increased Curie temperature and magnetization of the CCO layers in the superlattice. Therefore, we can expect each sample to have a different $M(T)$ dependence, and therefore also a different $K(T)$ dependence [55,58,31], resulting in a different T_R, as observed experimentally.

A further implication of our analysis is that the easy axis cannot be in any direction other than in plane or out of plane, since there are no other solutions than $\vartheta = 0$ and $\vartheta = \pi/2$. However, the magnitude of the effective anisotropy can change with temperature. To quantify this, we can calculate the difference between the maximum and minimum energy. In a system with uniaxial anisotropy, this would give the value of K. In our case, we obtain $\Delta E = E(0) - E(\pi/2) = -t_A K_A + t_B K_B$. This implies that for a fixed temperature and choice of materials, not only the sign, but also the absolute value of the magnetic anisotropy of the superlattice can be tuned through the choice of the thickness.

Finally, we discuss the limitations of this model. We have assumed that $J_{AB} \gg Kt$, which imposes $\vartheta_B = \vartheta_A - \pi$. This means that the magnetizations of the two layers can only be antiparallel, and not perpendicular to each other, as would be expected from the anisotropy of the single thin films. Our model therefore does not describe the case of orthogonal magnetizations. Nevertheless, we foresee that this might be observable in superlattices with much larger periodicity, where $J_{AB} \ll Kt$. For intermediate values of J_{AB}, it is not straightforward to develop an analytic solution, and a more complex magnetic configuration could occur. SQUID-VSM data for the superlattice SL 4/16 [Fig. 3(a)] indicate that this sample might already be thick enough to violate the condition $J_{AB} \gg Kt$. However, we do not have element-sensitive hysteresis loops for this sample, and further investigations would be needed to make a conclusive statement.

C. Comparison with other materials

We have realized an artificial metamaterial whose magnetic anisotropy and temperature dependence can be tuned by altering the design of the superlattice. While the magnetic anisotropy can also be tuned in magnetic metallic multilayers, such as Co/Pt, Co/Pd, Co/Au, and Co/Ni [59–61], superlattices consisting of insulating oxides are an appealing platform for magnonics. In this context, the control over anisotropy offers a way to influence the dispersion relation of spin waves.

Regarding oxides, the tuning of magnetic anisotropy has been reported in perovskite superlattices involving iridates [62,63] and/or ruthenates [64–66]. Here, the anisotropy is determined by the deformation of the oxygen octahedra [67] and asymmetric exchange at the interfaces [68], which are properties very specific to the interface of choice, so that it is difficult to apply this approach to other materials. In contrast, our approach relies on magnetostriction and symmetric exchange at the interfaces, which is applicable to a variety of materials. In particular, for our approach, the two layers in the superlattice should have the following properties: (i) orthogonal easy axes when grown on the same substrate, and (ii) different temperature dependences of their anisotropy, which is usually related to different T_C. With these conditions satisfied, the thickness of the layers provides a means to design the magnetic anisotropy at will. In addition, this method could be applied to superlattices composed of many other oxide layers, such as other spinel ferrites or garnets, in order to have a tunable magnetic anisotropy close to room temperature. In principle, this idea is also applicable to antiferromagnets, which are abundant amongst the magnetic oxides. Such a possibility to tailor the anisotropy in antiferromagnets is interesting, since the proposed spintronic devices are based on anisotropic magnetoresistance [69,70]. Spin-wave propagation in antiferromagnets also depends on the orientation of the Néel vector [71].

We have shown that we can engineer not only the direction of the easy axis at a fixed temperature, but also the temperature dependence of the anisotropy (by tuning the value of T_R). This feature might have interesting consequences for the switching of the magnetization state either through short light pulses [72,73] or electrical currents, which involve a change in the electronic temperature at the ps to fs timescale.

Finally, if the periodicity is increased, the interfacial exchange coupling is likely to become less important, and the magnetization of the two layers would not be necessarily antiparallel. In this case, it should be possible to stabilize noncollinear spin arrangements along the thickness of the superlattice. This would be particularly interesting in the presence of the interfacial Dzyaloshinskii-Moriya interaction, as it might result in the formation of topologically nontrivial spin textures in such an insulating metamaterial.

VI. CONCLUSIONS

In summary, we have synthesized $CoCr_2O_4/CoFe_2O_4$ (CCO/CFO) spinel superlattices with a superlattice period of few unit cells, and we have characterized their magnetic properties. The CCO layers in the superlattices have larger magnetic moments and higher Curie temperature compared to

the bulk, as demonstrated with XMCD measurements. This is due to the magnetic interactions at the interface, which is evidenced by the fact that the enhancement of the magnetic moment is more pronounced in samples with smaller periodicity. This interaction between the layers results in properties of the superlattices that are not trivially derived from those of bulk CCO and CFO. This is, for example, manifested in the magnetic anisotropy. Here, the magnetic easy axis is in plane at low temperature, as in CCO, and is out of plane at high temperature, as in CFO. The reorientation temperature T_R is determined by the period of the superlattice, and does not correspond to the Curie temperature of either the CCO or the CFO layers.

We have described the anisotropy of the superlattices with a simple analytical model taking into account the strain-induced anisotropy of the two layers and their magnetic interaction. The period of the superlattice determines the temperature dependence of the magnetic properties of the CCO and CFO layers. Taking this into account, the model can explain the trend of T_R across the series of samples analyzed.

Magnetic anisotropy plays a crucial role in the functionality of spintronic devices. For example, logic gates can be realized by laterally patterning magnetic anisotropy [74], and the ability to regulate the anisotropy over time is interesting for computation [75]. However, the requirements for the magnetic anisotropy limit the choice of materials available to build new devices with extended or improved functionality. Therefore, it is important to be able to engineer the anisotropy at the desired operational temperature, and a fine control of the anisotropy of the starting material is essential to be able to modulate it. Through the realization of superlattices with controlled periodicity, we provide a means to define the direction of the easy axis and adjust the magnitude of the magnetic anisotropy at a desired temperature, via tuning of T_R. We foresee that the same approach could be applied to a variety of other oxide systems with different magnetic properties, so opening the way to create devices based on anisotropy engineering.

The raw data files that support this study are available via the Zenodo repository [76].

ACKNOWLEDGMENTS

The x-ray absorption measurements were performed on the EPFL/PSI X-Treme beamline at the Swiss Light Source, Paul Scherrer Institut, Villigen, Switzerland. The authors would like to thank the Scientific Center for Optical and Electron Microscopy (ScopeM) at the ETH Zurich for their technical support. We also thank Milan Radovic, Daniele Pergolesi, Ekaterina Pomjakushina, and Marisa Medarde Barragan for stimulating scientific discussions. F.M. acknowledges funding from the European Union's Horizon 2020 research and innovation program, under the Marie Skłodowska-Curie Grant Agreement No. 884104 (PSI-FELLOW-III-3i).

[1] A. Fert, Nobel lecture: Origin, development, and future of spintronics, Rev. Mod. Phys. **80**, 1517 (2008).

[2] H. Ohno, M. D. Stiles, and B. Dieny, Spintronics, Proc. IEEE **104**, 1782 (2016).

[3] D. Sander, S. Valenzuela, D. Makarov, C. Marrows, E. Fullerton, P. Fischer, J. McCord, P. Vavassori, S. Mangin, P. Pirro *et al.*, The 2017 Magnetism Roadmap, J. Phys. D: Appl. Phys. **50**, 363001 (2017).

[4] S. Manipatruni, D. E. Nikonov, C. C. Lin, T. A. Gosavi, H. Liu, B. Prasad, Y. L. Huang, E. Bonturim, R. Ramesh, and I. A. Young, Scalable energy-efficient magnetoelectric spin–orbit logic, Nature (London) **565**, 35 (2019).

[5] J. G. Rau, E. K.-H. Lee, and H.-Y. Kee, Spin-orbit physics giving rise to novel phases in correlated systems: Iridates and related materials, Annu. Rev. Condens. Matter Phys. **7**, 195 (2016).

[6] J. M. D. M. Coey and C. L. Chien, Half-metallic ferromagnetic oxides, MRS Bull. **28**, 720 (2003).

[7] L. W. Martin and R. Ramesh, Multiferroic and magnetoelectric heterostructures, Acta Mater. **60**, 2449 (2012).

[8] C. Song, B. Cui, F. Li, X. Zhou, and F. Pan, Recent progress in voltage control of magnetism: Materials, mechanisms, and performance, Prog. Mater. Sci. **87**, 33 (2017).

[9] J. T. Heron, J. Bosse, Q. He, Y. Gao, M. Trassin, L. Ye, J. Clarkson, C. Wang, J. Liu, S. Salahuddin *et al.*, Deterministic switching of ferromagnetism at room temperature using an electric field, Nature (London) **516**, 370 (2014).

[10] F. Motti, G. Vinai, A. Petrov, B. A. Davidson, B. Gobaut, A. Filippetti, G. Rossi, G. Panaccione, and P. Torelli, Strain-induced magnetization control in an oxide multiferroic heterostructure, Phys. Rev. B **97**, 094423 (2018).

[11] A. Barman, G. Gubbiotti, S. Ladak, A. Adeyeye, M. Krawczyk, J. Grafe, C. Adelmann, S. Cotofana, A. Naeemi, V. Vasyuchka *et al.*, The 2021 Magnonics Roadmap, J. Phys.: Condens. Matter **33** 413001 (2021).

[12] W. Chen and M. Sigrist, Dissipationless Multiferroic Magnonics, Phys. Rev. Lett. **114**, 157203 (2015).

[13] E. Dagotto, T. Hotta, and A. Moreo, Colossal magnetoresistant materials: The key role of phase separation, Phys. Rep. **344**, 1 (2001).

[14] M. Coll, J. Fontcuberta, M. Althammer, M. Bibes, H. Boschker, A. Calleja, G. Cheng, M. Cuoco, R. Dittmann, B. Dkhil *et al.*, Towards oxide electronics: A roadmap, Appl. Surf. Sci. **482**, 1 (2019).

[15] M. Kadic, G. W. Milton, M. van Hecke, and M. Wegener, 3D metamaterials, Nat. Rev. Phys. **1**, 198 (2019).

[16] H. Wang, F. Tang, P. H. Dhuvad, and X. Wu, Interface enhanced functionalities in oxide superlattices under mechanical and electric boundary conditions, npj Comput. Mater. **6**, 52 (2020).

[17] R. Ramesh and D. G. Schlom, Creating emergent phenomena in oxide superlattices, Nat. Rev. Mater. **4**, 257 (2019).

[18] H. Y. Hwang, Y. Iwasa, M. Kawasaki, B. Keimer, N. Nagaosa, and Y. Tokura, Emergent phenomena at oxide interfaces, Nat. Mater. **11**, 103 (2012).

[19] H. Chen and A. Millis, Charge transfer driven emergent phenomena in oxide heterostructures, J. Phys.: Condens. Matter **29**, 243001 (2017).

[20] J. A. Mundy, C. Brooks, M. Holtz, J. Moyer, H. Das, A. Rébola, J. Heron, J. Clarkson, S. Disseler, Z. Liu *et al.*, Atomically engineered ferroic layers yield a room-temperature magnetoelectric multiferroic, Nature (London) **537**, 523 (2016).

[21] A. K. Yadav, C. Nelson, S. Hsu, Z. Hong, J. Clarkson, C. Schlepuëtz, A. Damodaran, P. Schafer, E. Arenholz, L. Dedon *et al.*, Observation of polar vortices in oxide superlattices, Nature (London) **530**, 198 (2016).

[22] C. Domínguez, A. B. Georgescu, B. Mundet, Y. Zhang, J. Fowlie, A. Mercy, A. Weelchli, S. Catalano, D. T. L. Alexander, P. Ghosez *et al.*, Length scales of interfacial coupling between metal and insulator phases in oxides, Nat. Mater. **19**, 1182 (2020).

[23] K. Ueda, H. Tabata, and T. Kawai, Control of magnetic properties in $LaCrO_3$–$LaFeO_3$ artificial superlattices, J. Appl. Phys. **89**, 2847 (2001).

[24] X. Liu, S. Singh, V. Drouin-Touchette, T. Asaba, J. Brewer, Q. Zhang, Y. Cao, B. Pal, S. Middey, P. S. A. Kumar *et al.*, Proximate quantum spin liquid on designer lattice, Nano Lett. **21**, 2010 (2021).

[25] D. Yi, Y. Wang, O. M. J. van't Erve, L. Xu, H. Yuan, M. J. Veit, P. P. Balakrishnan, Y. Choi, A. T. N'Daye, P. Shafer *et al.*, Emergent electric field control of phase transformation in oxide superlattices, Nat. Commun. **11**, 902 (2020).

[26] X. Liu, S. Singh, B. J. Kirby, Z. Zhong, Y. Cao, B. Pal, M. Kareev, S. Middey, J. W. Freeland, P. Shafer *et al.*, Emergent magnetic state in (111)-oriented quasi-two-dimensional spinel oxides, Nano Lett. **19**, 8381 (2019).

[27] X. Liu, D. Choudhury, Y. Cao, S. Middey, M. Kareev, D. Meyers, J.-W. Kim, P. Ryan, and J. Chakhalian, Epitaxial growth of (1 1 1)-oriented spinel $CoCr_2O_4/Al_2O_3$ heterostructures, Appl. Phys. Lett. **106**, 071603 (2015).

[28] H. Yahiro, H. Tanaka, Y. Yamamoto, and T. Kawai, Construction of $ZnFe_2O_4/ZnGa_2O_4$ spinel-type artificial superlattice by pulsed laser deposition, Jpn. J. Appl. Phys. **41**, 5153 (2002).

[29] T. Murata, Y. Kozuka, M. Uchida, and M. Kawasaki, Magnetic Properties of Spin Frustrated Spinel $ZnFe_2O_4/ZnCr_2O_4$ Superlattices, J. Appl. Phys. **118**, 193901 (2015).

[30] R. Guzman, J. Heuver, S. Matzen, C. Magén, and B. Noheda, Structural and magnetic properties of [001] $CoCR_2O_4$ thin films, Phys. Rev. B **96**, 104105 (2017).

[31] See Supplemental Material at http://link.aps.org/supplemental/10.1103/PhysRevB.108.104426 for the estimation of the K and J parameters, extended SQUID-VSM data for doped samples and thin films, resonant scattering measurements of CCO thin films, estimate of the stoichiometry of thin films, XMCD experimental details and extended data, and extended transmission electron microscopy data.

[32] Y. Yamasaki, S. Miyasaka, Y. Kaneko, J.-P. He, T. Arima, and Y. Tokura, Magnetic Reversal of the Ferroelectric Polarization in a Multiferroic Spinel Oxide, Phys. Rev. Lett. **96**, 207204 (2006).

[33] K. L. Choy, Chemical vapour deposition of coatings, Prog. Mater. Sci. **48**, 57 (2003).

[34] Y. J. Choi, J. Okamoto, D. J. Huang, K. S. Chao, H. J. Lin, C. T. Chen, M. van Veenendaal, T. A. Kaplan, and S. W. Cheong, Thermally or Magnetically Induced Polarization Reversal in the Multiferroic $CoCr_2O_4$, Phys. Rev. Lett. **102**, 067601 (2009).

[35] G. Shirane, D. E. Cox, and S. J. Pickart, Magnetic structures in $FeCr_2S_4$ and $FeCr_2O_4$, J. Appl. Phys. **35**, 954 (1964).

[36] T. A. Kaplan and N. Menyuk, Spin ordering in three-dimensional crystals with strong competing exchange interactions, Philos. Mag. **87**, 3711 (2007).

[37] N. Ortiz Hernández, S. Parchenko, J. R. L. Mardegan, M. Porer, E. Schierle, E. Weschke, M. Ramakrishnan, M. Radovic, J. A. Heuver, B. Noheda *et al.*, Magnetic field dependent cycloidal rotation in pristine and Ge-doped $CoCr_2O_4$, Phys. Rev. B **103**, 085123 (2021).

[38] S. Matzen, J.-B. Moussy, R. Mattana, F. Petroff, C. Gatel, B. Warot-Fonrose, J. C. Cezar, A. Barbier, M.-A. Arrio, and P. Sainctavit, Restoration of bulk magnetic properties by strain engineering in epitaxial $CoFe_2O_4$ (001) ultrathin films, Appl. Phys. Lett. **99**, 052514 (2011).

[39] J. A. Heuver, A. Scaramucci, Y. Blickenstorfer, S. Matzen, N. A. Spaldin, C. Ederer, and B. Noheda, Strain-induced magnetic anisotropy in epitaxial thin films of the spinel $CoCr_2O_4$, Phys. Rev. B **92**, 214429 (2015).

[40] D. Fritsch and C. Ederer, First-principles calculation of magnetoelastic coefficients and magnetostriction in the spinel ferrites $CoFe_2O_4$ and $NiFe_2O_4$, Phys. Rev. B **86**, 014406 (2012).

[41] R. Padam, S. Pandya, S. Ravi, A. K. Nigam, S. Ramakrishnan, A. K. Grover, and D. Pal, Magnetic compensation effect and phase reversal of exchange bias field across compensation temperature in multiferroic $Co(Cr_{0.95}Fe_{0.05})_2O_4$, Appl. Phys. Lett. **102**, 112412 (2013).

[42] R. Kumar, S. K. Upadhyay, Y. Xiao, W. Ji, and D. Pal, Influence of Fe substitution on multiferrocity and magneto-dielectric properties in $CoCr_2O_4$, J. Phys. D: Appl. Phys. **51**, 385001 (2018).

[43] C. L. Li, T. Y. Yan, G. O. Barasa, Y. H. Li, R. Zhang, Q. S. Fu, X. H. Chen, and S. L. Yuan, Negative magnetization and exchange bias effect in Fe-doped $CoCr_2O_4$, Ceram. Int. **44**, 15446 (2018).

[44] C. Piamonteze, U. Flechsig, S. Rusponi, J. Dreiser, J. Heidler, M. Schmidt, R. Wetter, M. Calvi, T. Schmidt, H. Pruchova *et al.*, X-Treme Beamline at SLS: X-ray magnetic circular and linear dichroism at high field and low temperature, J. Synchrotron Rad. **19**, 661 (2012).

[45] C. Piamonteze, Y. W. Windsor, S. R. V. Avula, E. Kirk, and U. Staub, Soft X-ray absorption of thin films detected using substrate luminescence: A performance analysis, J. Synchrotron Radiat. **27**, 1289 (2020).

[46] Y. W. Windsor, C. Piamonteze, M. Ramakrishnan, A. Scaramucci, L. Rettig, J. A. Heuver, E. M. Bothschafter, N. S. Bingham, A. Alberca, S. R. V. Avula *et al.*, Magnetic properties of strained multiferroic $CoCr_2O_4$: A soft x-ray study, Phys. Rev. B **95**, 224413 (2017).

[47] R. V. Chopdekar, M. Liberati, Y. Takamura, L. F. Kourkoutis, J. S. Bettinger, B. B. Nelson-Cheesman, E. Arenholz, A. Doran, A. Scholl, D. A. Muller *et al.*, Magnetism at spinel thin film interfaces probed through soft x-ray spectroscopy techniques, J. Magn. Magn. Mater. **322**, 2915 (2010).

[48] K. Dwight and N. Menyuk, Distant-neighbor B-B interactions in cobalt chromite, J. Appl. Phys. **40**, 1156 (1969).

[49] P. G. Bercoff and H. R. Bertorello, Exchange constants and transfer integrals of spinel ferrites, J. Magn. Magn. Mater **169**, 314 (1997).

[50] C. Ederer and M. Komelj, Magnetic coupling in $CoCr_2O_4$ and $MnCr_2O_4$: An LSDA+U study, Phys. Rev. B **76**, 064409 (2007).

[51] M. Huijben, L. W. Martin, Y.-H. Chu, M. B. Holcomb, P. Yu, G. Rijnders, D. H. A. Blank, and R. Ramesh, Critical thickness and orbital ordering in ultrathin $La_{0.7}Sr_{0.3}MnO_3$ films, Phys. Rev. B **78**, 094413 (2008).

[52] A. Zakharova, M. Caputo, E. B. Guedes, M. Radovic, F. Nolting, and C. Piamonteze, Interplay between magnetism and interface-induced effects in ultrathin manganites, Phys. Rev. Mater. **5**, 124404 (2021).

[53] G. De Luca, J. Spring, M. Kaviani, S. Jöhr, M. Campanini, A. Zakharova, C. Guillemard, J. Herrero-Martin, R. Erni, C. Piamonteze *et al.*, Top-layer engineering reshapes charge transfer at polar oxide interfaces, Adv. Mater. **34**, 2203071 (2022).

[54] F. C. Voogt, T. T. M. Palstra, L. Niesen, O. C. Rogojanu, M. A. James, and T. Hibma, Superparamagnetic behavior of structural domains in epitaxial ultrathin magnetite films, Phys. Rev. B **57**, R8107(R) (1998).

[55] J. M. D. Coey, *Magnetism and Magnetic Materials* (Cambridge University Press, New York, 2001).

[56] J. Stöhr and H. C. Siegmann, *Magnetism: From Fundamentals to Nanoscale Dynamics* (Springer, Berlin, Heidelberg, 2006).

[57] E. Du Trémolet de Lacheisserie, D. Gignoux, and M. Schlenker, *Magnetism* (Springer, Boston, 2005).

[58] J. B. Staunton, L. Szunyogh, A. Buruzs, B. L. Gyorffy, S. Ostanin, and L. Udvardi, Temperature dependence of magnetic anisotropy: An *ab initio* approach, Phys. Rev. B **74**, 144411 (2006).

[59] B. N. Engel, C. D. England, R. A. Van Leeuwen, M. H. Wiedmann, and C. M. Falco, Interface Magnetic Anisotropy in Epitaxial Superlattices, Phys. Rev. Lett. **67**, 1910 (1991).

[60] C. H. Lee, H. He, F. J. Lamelas, W. Vavra, C. Uher, and R. Clarke, Magnetic anisotropy in epitaxial Co superlattices, Phys. Rev. B **42**, 1066 (1990).

[61] C. J. Lin, G. L. Gorman, C. H. Lee, R. F. C. Farrow, E. E. Marinero, H. V. Do, H. Notarys, and C. J. Chien, Magnetic and structural properties of Co/Pt multilayers, J. Magn. Magn. Mater. **93**, 194 (1991).

[62] D. Yi, H. Amari, P. P. Balakrishnan, C. Klewe, A. T. N'Diaye, P. Shafer, N. Browning, and Y. Suzuki, Enhanced Interface-Driven Perpendicular Magnetic Anisotropy by Symmetry Control in Oxide Superlattices, Phys. Rev. Appl. **15**, 024001 (2021).

[63] Z. Lu, J. Liu, L. Wen, J. Feng, S. Kong, X. Zheng, S. Li, P. Jiang, Z. Zhong, J. Zhu *et al.*, Lateral modulation of magnetic anisotropy in tricolor 3d-5d oxide superlattices, ACS Appl. Electron. Mater. **3**, 4210 (2021).

[64] Z. Zeng, J. Feng, X. Zheng, C. Wang, J. Liu, Z. Lu, F.-X. Jiang, X.-H. Xu, Z. Wang, and R.-W. Li, Emergent ferromagnetism with tunable perpendicular magnetic anisotropy in short-periodic $SrIrO_3/SrRuO_3$ superlattices, Appl. Phys. Lett. **116**, 142401 (2020).

[65] L. Qu, D. Lan, K. Zhang, E. Hua, B. Ge, L. Xu, F. Jin, G. Gao, L. Wang, and W. Wu, Continuous tunable lateral magnetic anisotropy in $La_{0.67}Ca_{0.33}MnO_3/SrRuO_3$ superlattices by stacking period-modulation, AIP Adv. **11**, 075001 (2021).

[66] Z. Guo, D. Lan, L. Qu, K. Zhang, F. Jin, B. Chen, S. Jin, G. Gao, G. Chen, L. Wang *et al.*, Control of ferromagnetism and magnetic anisotropy via tunable electron correlation and spin-orbital coupling in $La_{0.67}Ca_{0.33}MnO_3/Ca(Ir, Ru)O_3$ superlattices, Appl. Phys. Lett. **113**, 231601 (2018).

[67] D. Yi, C. L. Flint, P. P. Balakrishnan, K. Mahalingam, B. Urwin, A. Vailionis, A. T. N'Diaye, P. Shafer, E. Arenholz, Y. Choi *et al.*, Tuning Perpendicular Magnetic Anisotropy by Oxygen Octahedral Rotations in $(La_{1-X}Sr_xMnO_3)/(SrIrO_3)$ Superlattices, Phys. Rev. Lett. **119**, 077201 (2017).

[68] D. Yia, J. Liu, S. L. Hsu, L. Zhang, Y. Choi, J. W. Kim, Z. Chen, J. D. Clarkson, C. R. Serrao, E. Arenholz *et al.*, Atomic-scale control of magnetic anisotropy via novel spin-orbit coupling effect in $La_{2/3}Sr_{1/3}MnO_3/SrIrO_3$ superlattices, Proc. Natl. Acad. Sci. USA **113**, 6397 (2016).

[69] T. Jungwirth, X. Marti, P. Wadley, and J. Wunderlich, Antiferromagnetic spintronics, Nat. Nanotechnol. **11**, 231 (2016).

[70] P. Wadley, B. Howells, J. Železný , C. Andrews, V. Hils, R. P. Campion, V. Novák, F. Freimuth, Y. Mokrousov, A. W. Rushforth *et al.*, Electrical switching of an antiferromagnet, Science **351**, 587 (2016).

[71] R. Lebrun, A. Ross, S. A. Bender, A. Qaiumzadeh, L. Baldrati, J. Cramer, A. Brataas, R. A. Duine, and M. Kläui, Tunable long-distance spin transport in a crystalline antiferromagnetic iron oxide, Nature (London) **561**, 222 (2018).

[72] S. Parchenko, N. Ortiz Hernandez, M. Savoini, M. Porer, M. Decker, B. Burganov, E. M. Bothschafter, C. Dornes, Y. W. Windsor, M. Ramakrishnan *et al.*, Ultrafast probe of magnetization dynamics in multiferroic $CoCr_2O_4$ and $Co_{0.975}Ge_{0.025}Cr_2O_4$, Phys. Rev. B **105**, 064432 (2022).

[73] R. Takahashi, Y. Tani, H. Abe, M. Yamasaki, I. Suzuki, D. Kan, Y. Shimakawa, and H. Wadati, Ultrafast demagnetization in $NiCo_2O_4$ thin films probed by time-resolved microscopy, Appl. Phys. Lett. **119**, 102404 (2021).

[74] Z. Luo, A. Hrabec, T. P. Dao, G. Sala, S. Finizio, J. Feng, S. Mayr, J. Raabe, P. Gambardella, and L. J. Heyderman, Current-driven magnetic domain-wall logic, Nature (London) **579**, 214 (2020).

[75] C. Yun, Z. Liang, A. Hrabec, Z. Liu, M. Huang, L. Wang, Y. Xiao, Y. Fang, W. Li, W. Yang *et al.*, Electrically programmable magnetic coupling in an Ising network exploiting solid-state ionic gating, arXiv:2305.03422.

[76] V. Scagnoli, "Effect of periodicity on the magnetic anisotropy in spinel oxide superlattices (2023)", doi:10.5281/zenodo.8314283.